



Mathematical Simulation of Decarburization with CO₂ Injection During RH Refining of Ultra-Low-Carbon Steel

Gujun Chen¹ · Jiang Yang² · Yugang Li² · Shengping He²

Received: 6 November 2023 / Accepted: 20 February 2024
© The Author(s) under exclusive licence to The Korean Institute of Metals and Materials 2024

Abstract

The iron and steel industry is addicted to the resource utilization of carbon dioxide (CO₂) produced by themselves. In this study, a mathematical model, based on tanks-in-series model, is developed to describe Ruhrstahl–Heraeus (RH) decarburization during ultra-low-carbon steel refining process when CO₂ is injected as the lift gas, and the CO₂ bubble surface, bath surface, droplet surface, and bulk steel are selected as decarburization reaction sites. The variation of vacuum chamber pressure during vacuum pumping process can be calculated directly from the mathematical model, and thus, the influence of variation of vacuum chamber pressure on flow and mixing of molten steel as well as decarburization reaction can be considered. The predicted variations in the vacuum chamber pressure and dissolved C and O contents in the molten steel are consistent with industrial data. Simulation results indicate that, compared with Ar injection, the final dissolved C and O contents are respectively increased from 9 and 367 ppm to 20 and 446 ppm for CO₂ injection. Therefore, CO₂ can be used to completely replace traditional Ar to meet the requirement of a final dissolved C content in molten steel of less than 20 ppm when the initial dissolved C content is 200 ppm and the initial dissolved O content is greater than or equal to 600 ppm. If lower dissolved C and O contents in the molten steel are required at the end, a switching operation from CO₂ to Ar injection at the middle stage of decarburization can be performed.

Keywords RH · Decarburization · Ultra-low-carbon steel · Carbon dioxide · Mathematical model

1 Introduction

With rapid industrialization, global carbon dioxide (CO₂) emissions have increased by 61% over the last 30 years, reaching 36.3 billion tons by 2021 [1]. As one of the largest emission sources, the iron and steel industry has been responsible for 8% of the anthropogenic CO₂ emissions and 25% of the industrial CO₂ emissions in recent years [2].

Therefore, it is particularly urgent and significant to reduce CO₂ emissions or utilize CO₂ in the iron and steel industry [3, 4], and the resource utilization of CO₂ in steelmaking and refining processes has received more attention.

CO₂ utilization in the steelmaking process has been studied by many scholars, as recently reviewed by Dong et al. [5] On one hand, the dissolved C in the molten bath can directly react with CO₂, which not only reduces the dissolved C content but also strengthens bath stirring by generating more carbon monoxide (CO). However, the reactions of CO₂ with the elements in the molten bath are endothermic or slightly exothermic, which favors control of the bath temperature. For these reasons, the utilization of CO₂ in basic oxygen furnace steelmaking has attracted the attention of many researchers [6–10], and very promising results have been produced in terms of the control of the dust amount, iron loss, phosphorus and nitrogen contents in the molten bath, and the slag-splashing process, as well as economic and environmental benefits. In addition, the utilization of CO₂ in electric arc furnace steelmaking has also attracted attention [11, 12], and it has been demonstrated that suitable

✉ Yugang Li
liy7408@163.com

✉ Shengping He
heshp@cqu.edu.cn

Gujun Chen
chengujun@yznu.edu.cn

Jiang Yang
jiang_0y@163.com

¹ College of Materials Science and Engineering, Yangtze Normal University, Fuling 408100, China

² College of Materials Science and Engineering, Chongqing University, Chongqing 400044, China

kinetic and thermodynamic conditions for carbon–oxygen, desulfurization, and dephosphorization reactions could be provided, and the dissolved N content and dust production could be decreased.

CO₂ utilization in the refining process has largely focused on the Ruhrstahl–Heraeus (RH) vacuum refining process, although CO₂ utilization in argon oxygen decarburization refining [13, 14] and ladle furnace refining [15] also attracted some research attention. The RH vacuum degasser is an essential tool for removing dissolved C from molten steel during ultra-low-carbon steel production [16–19]. Ar gas is injected as the power source for steel circulation under vacuum conditions, and the decarburization reaction occurs at the Ar bubble surface, bath surface, splash droplet surface, and bulk steel near the bath surface [20–22].

The concept of substituting Ar gas with CO₂ as the lift gas of the RH degassing process was first reported by Zhu et al. [23] from the aspect of thermodynamic analysis in 2017; subsequently, industrial experiments were conducted to study the selective oxidation of dissolved C and Al in low-carbon steel by injecting CO₂ [24–27]. In their experiments, Al was added for deoxidation before the RH process, and the initial dissolved C and Al contents were 1280–1310 ppm and 210–428 ppm, respectively. The experimental results indicated that CO₂ mainly reacted with dissolved C when the dissolved Al content was less than a certain value; otherwise, a large amount of dissolved Al could be oxidized by CO₂ after the RH process. In addition, an equivalent or even better dehydrogenation effect was achieved, and only a slight increase in the temperature drop of the molten steel was observed in comparison with Ar injection. Therefore, they suggested that CO₂ could be used to replace Ar gas during the RH degassing of low-carbon steel by reducing the initial dissolved Al content and secondarily adding Al during the late stage of RH degassing.

Compared with the low-carbon steel degassing process studied by Zhu et al. [24–27], the ultra-low-carbon steel degassing process was completely different. For ultra-low-carbon steel degassing, the dissolved C content must be reduced from 150 to 300 ppm to less than 20 or even 10 ppm through the carbon–oxygen reaction in the RH degasser. The first investigation of ultra-low-carbon steel degassing with CO₂ injection was thermodynamically performed by the present authors [28, 29]. The results showed that the CO generated by CO₂ decomposition further decomposed into dissolved C and O when the dissolved C content was lower than a certain value, which increased the dissolved C content during the late stage of RH degassing. Because CO decomposition at the CO₂ bubble surface and CO formation at other reaction sites could occur simultaneously in the late stage of RH decarburization, it was still unknown how the dissolved C content in the entire RH degasser would be influenced by CO₂ injection. This serious challenge can

be addressed by mathematical simulation, which has been widely adopted to understand RH decarburization with traditional Ar injection [30–32]. It should be noted that the vacuum chamber pressure was treated as a constant in most of the previous mathematical models [20–22] and thus the variation of vacuum chamber pressure during vacuum pumping process on flow, mixing and decarburization was ignored. In addition, the influence of the variation of vacuum chamber pressure was considered in some mathematical models [30–32], in which the pressure variation measured from the industrial experiment was used as the boundary condition of mathematical model. However, none of the previous mathematical models can directly calculate the variation of vacuum chamber pressure.

In this study, a mathematical model, based on tanks-in-series model, is developed to study RH decarburization with CO₂ injection during ultra-low-carbon steel degassing. The decarburization reactions occurring at the CO₂ bubble surface, bath surface, splash droplet surface, and bulk steel are integrated. Unlike the previous mathematical models, the variation of vacuum chamber pressure during vacuum pumping process can be calculated directly in this model, and thus the influence of pressure variation on decarburization can be considered. The predicted vacuum chamber pressure and dissolved C and O contents are compared with those observed in industrial experiments. Based on the model, the decarburization performances of CO₂ and Ar injections are discussed and compared. The decarburization performances at different initial dissolved O contents are investigated. A switching operation from pure CO₂ to pure Ar injection in the middle stage of decarburization is also proposed to decrease the dissolved C and O contents.

2 Mathematical Model

A mathematical model, based on tanks-in-series model, is developed to investigate the decarburization kinetics of the RH degasser with CO₂ injection. The decarburization reaction at the surface of CO₂ bubbles, at the bath and droplet surfaces in vacuum chamber, and at the bulk steel of vacuum chamber are integrated, and FeO decomposition reaction in ladle is also considered.

2.1 Tanks-in-Series Model

2.1.1 Description of Water Model Experiment

The circulation flow rate and mixing time of molten steel in the RH degasser are important parameters for the decarburization dynamical model. In this study, a water model of 1/5 linear scale for a 220-ton industrial RH degasser is established according to the geometric similarity, vacuum

degree similarity, and Froude number similarity, and the details of similarity criteria can refer to the studies by Wang et al. [33] and Wang et al. [34]. The schematic diagram of water model and the geometric dimensions and physical parameters of the RH degasser are shown in Fig. 1 and Table 1, respectively. As indicated in Fig. 1, a conductivity meter is used to determine the mixing time by analyzing the NaCl concentration (NaCl-saturated solution is introduced from the vacuum chamber) in water, and a current meter is used to estimate the circulation flow rate by measuring the water velocity. Based on the similarity criteria, the circulation flow rate and mixing time measured from water model experiment can then be converted to those of the industrial RH degasser.

2.1.2 Description of Tanks-in-Series Model

The whole RH degasser is divided into four parts (up-snorkel, vacuum chamber, down-snorkel, and ladle) in series, and each part consists of several completely-mixed tanks for lift gas, molten steel or molten slag in series, as illustrated

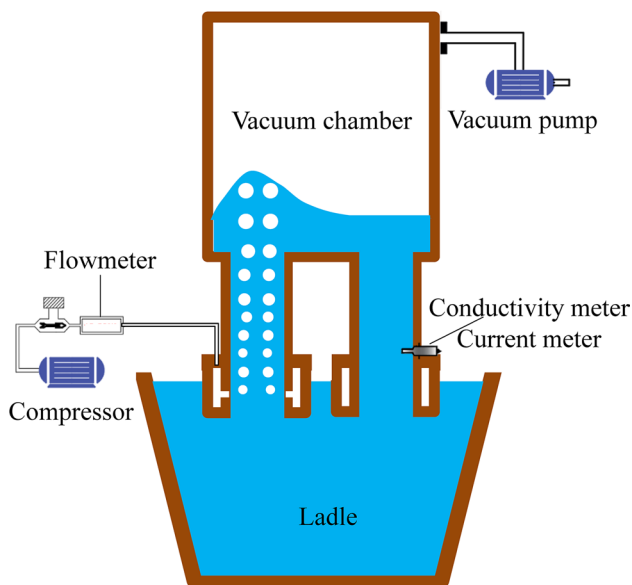


Fig. 1 Schematic representation of water model experiment

Table 1 Geometric dimensions and physical parameters of the RH degasser

	Industrial RH degasser	Water model
Top/bottom diameter of ladle, mm	3837/3200	767.4/640
Height of ladle, mm	4400	880
External/internal diameter of snorkels, mm	1340/680	268/136
Height of snorkels, mm	1600	320
Diameter/height of vacuum chamber, mm	2340/6280	468/1256
Density of molten steel/molten slag/water, kg/m ³	7020/3500/998.2	
Density of Ar/CO ₂ /air at standard state, kg/m ³	1.784/1.977/1.293	

in Fig. 2. The circulation flow rate of molten steel converted from the water model experiment is inputted for the mass transfer between two adjacent tanks for molten steel, and the mixing time of molten steel can then be calculated by introducing the tracer and monitoring the variation of tracer concentration.

Except the flow and mixing of molten steel, decarburization reaction can occur inside the tanks for molten steel as well as at the interface between the tanks for molten steel and lift gas. In addition, FeO decomposition reaction can occur at the interface between the tanks for molten steel and molten slag. Details of chemical reaction will be described in Sect. 2.2.

In this study, the influence of the number of tanks for molten steel in different parts on mixing time of molten steel in the whole RH degasser is numerically investigated. It is found that the mixing time is scarcely influenced by the number of tanks in up-snorkel, down-snorkel, and vacuum chamber as a result of the strong stirring of molten steel in these parts, while it is significantly determined by the number of tanks in ladle due to the existence of a huge recirculation zone with weak turbulence in this part. The influence of the number of tanks in ladle on mixing time of molten steel in the RH degasser is shown in Fig. 3, in which the number of tanks for molten steel in other parts is set to 1. Clearly, less tanks in a certain part mean that the molten steel in that part can mix more faster, and the calculated mixing time is in agreement with the results converted from the water model experiment when the number of tanks for molten steel in ladle is set to 4.

The number of tanks in up-snorkel and vacuum chamber can be set to 1 if only the mixing time of molten steel is considered. However, the chemical reaction also needs to be taken into account. In this study, the influence of number of tanks in each part on decarburization performance of the RH degasser is also numerically investigated, and the appropriate number of tanks in each part is listed in Table 2.

Fig. 2 Schematic representation of tanks-in-series model for the RH degasser

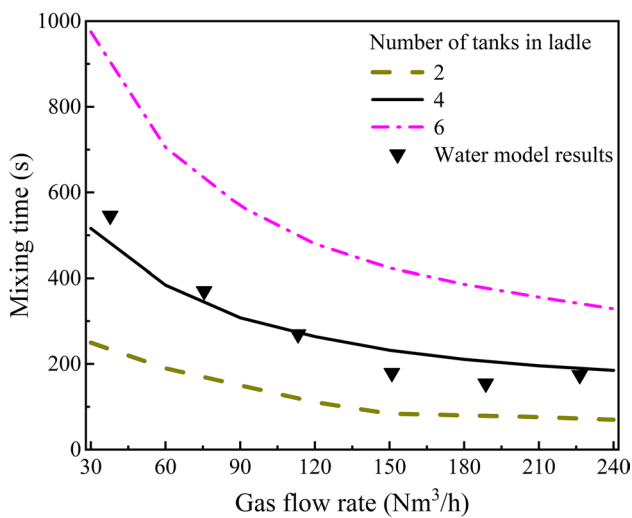
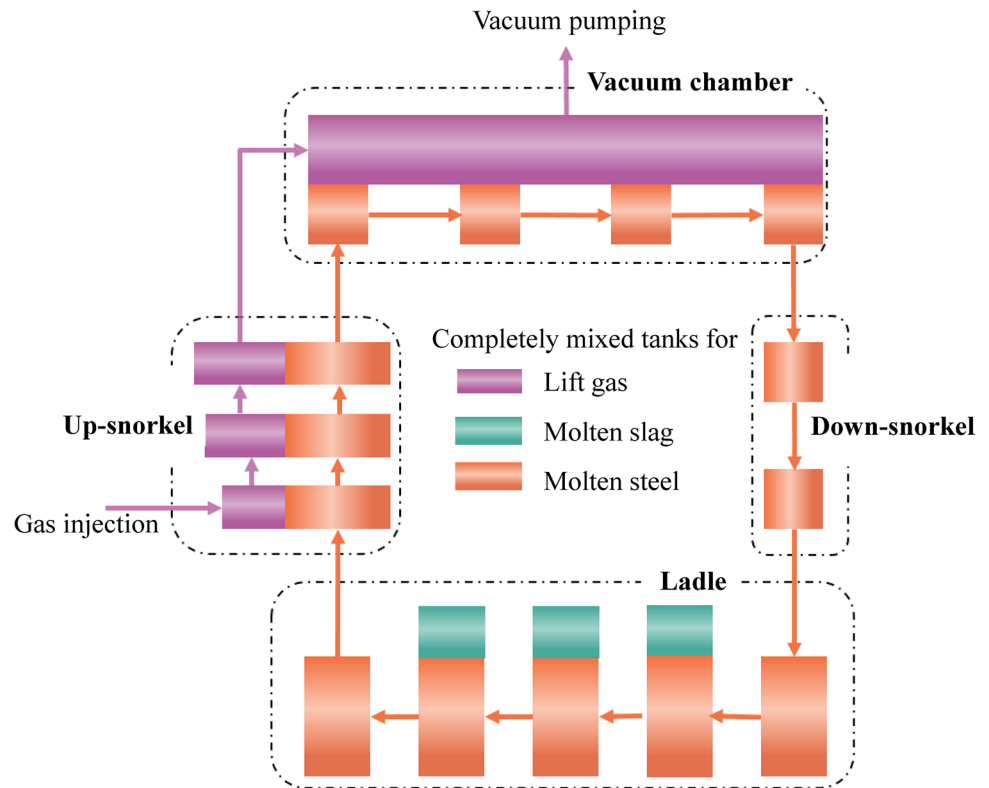


Fig. 3 Effect of number of tanks for molten steel in ladle on calculated mixing time, accompanied with the results converted from the water model experiment. Mixing time is defined as the time when tracer concentration in molten steel falls into the range of $\pm 3\%$ of the final concentration

Table 2 Number of completely-mixed tanks in each part

Up-snorkel	Lift gas	8
	Molten steel	8
Vacuum chamber	Lift gas	1
	Molten steel	2
Down-snorkel	Molten steel	1
Ladle	Molten slag	2
	Molten steel	4

into dissolved O and CO in the following form [35]:



$$\log K_1 = \log \left(\frac{(P_{CO}/P^\ominus)(f_O [\text{wt}\% O])}{(P_{CO_2}/P^\ominus)} \right) = -\frac{8718}{T} + 4.762 \quad (2)$$

The reaction of the dissolved O produced in Eq. 1 with C dissolved in molten steel can be written in the following form [35]:



2.2 Thermodynamics of Chemical Reactions

2.2.1 Decarburization reaction

When CO₂ bubbles are injected as lift gas, they decompose

$$\log K_2 = \log \left(\frac{(P_{CO}/P^\ominus)}{(f_C[\text{wt}\% C])(f_O[\text{wt}\% O])} \right) = \frac{1160}{T} + 2.003 \quad (4)$$

The combination of Eqs. 1 and 3 yields Eq. 5 in the following form [35]:



$$\log K_3 \left(= \frac{(P_{CO}/P^\ominus)^2}{(f_C[\text{wt}\% C])(P_{CO_2}/P^\ominus)} \right) = -\frac{7558}{T} + 6.765 \quad (6)$$

Therefore, Eq. 5 can occur at CO₂ bubble surface, bath surface, and droplet surface. Simultaneously, the reaction of the dissolved C and O contained in the molten steel itself, according to Eq. 3, can occur at the CO₂ bubble surface, bath surface, droplet surface, and bulk steel. The decarburization reaction mechanism is shown in Fig. 4 with sites 1–4.

2.2.2 FeO decomposition reactions

As shown in Fig. 4 with site 5, the FeO contained in the ladle slag can decompose at the steel–slag interface, and the dissolved O can be transferred to the molten steel [36].



$$\log K_4 = \log \left(\frac{(f_O[\text{wt}\% O])}{\alpha_{\text{FeO}}} \right) = -\frac{6150}{T} + 2.604 \quad (8)$$

In Eqs. 1–8, square bracket [] indicates the dissolved species in molten steel, and subscript *g* indicates the gas phases. *P*[⊖] is the standard atmospheric pressure (Pa), *P*_{CO} and *P*_{CO₂}

are the CO and CO₂ partial pressures, respectively (Pa). *K* is the reaction equilibrium constant. [wt% C] and *f*_C (≈1) are the mass percentage and activity coefficient of dissolved C, respectively; and [wt% O] and *f*_O (≈1) are the mass percentage and activity coefficient of dissolved O, respectively. α_{FeO} is the activity of FeO in the ladle slag, which was calculated using the FactSage thermodynamic software.

2.3 Basic Equations

The mass balance of dissolved C and O for each completely-mixed tank in the up-snorkel, vacuum chamber, down-snorkel, and ladle can be written separately in the following form:

$$w_{U,i} \frac{d[\text{wt}\% E]}{dt} = Q_1([\text{wt}\% E]_j - [\text{wt}\% E]_i) - v_{\text{bubb},E} M_E \quad (9)$$

$$w_{V,i} \frac{d[\text{wt}\% E]}{dt} = Q_1([\text{wt}\% E]_j - [\text{wt}\% E]_i) - (v_{\text{bath},E} + v_{\text{drop},E} + v_{\text{bulk},E}) M_E \quad (10)$$

$$w_{D,i} \frac{d[\text{wt}\% E]}{dt} = Q_1([\text{wt}\% E]_j - [\text{wt}\% E]_i) \quad (11)$$

$$w_{L,i} \frac{d[\text{wt}\% E]}{dt} = Q_1([\text{wt}\% E]_j - [\text{wt}\% E]_i) + v_{\text{slag},E} M_E \quad (12)$$

In Eqs. 9–12, the capital letter *E* represents the dissolved elements C and O. The subscripts *i* and *j* indicate two adjacent completely-mixed tanks, and subscripts *U*, *V*, *D*, and *L* indicate the up-snorkel, vacuum chamber, down-snorkel, and ladle, respectively. *M*_E is the molar mass of element *E* (kg/mol). *w*_{U,i}, *w*_{V,i}, *w*_{D,i}, and *w*_{L,i} are the steel weights (kg) for tank *i* in the up-snorkel, vacuum chamber, down-snorkel, and ladle, respectively. It should be pointed out that, for simplification, the zone with CO₂ bubbles in chamber vacuum above the up-snorkel is assigned to the up-snorkel, as schematically shown in Fig. 4, and therefore this zone must be excluded from the decarburization reaction at bulk steel in vacuum chamber. *Q*₁ indicates the circulation flow rate of molten steel (kg/s) during the RH degassing, which is converted from the water model experiment in Sect. 2.1. *v*_{m,E} is the chemical reaction rate of the dissolved element *E* at site *m* (mol/s), which is calculated in Sect. 2.4.

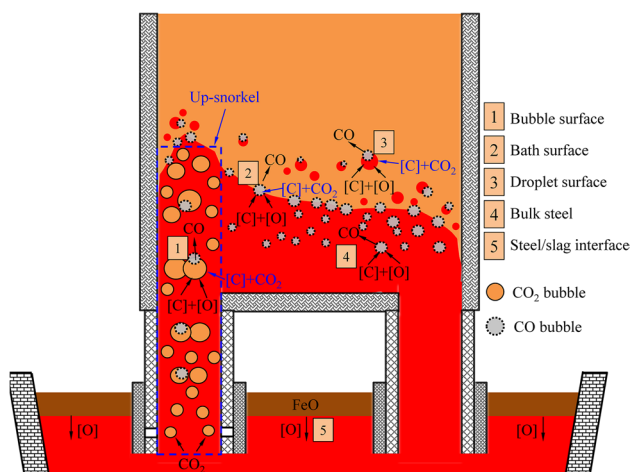


Fig. 4 Diagram of chemical reaction at each site during RH decarburization with CO₂ injection

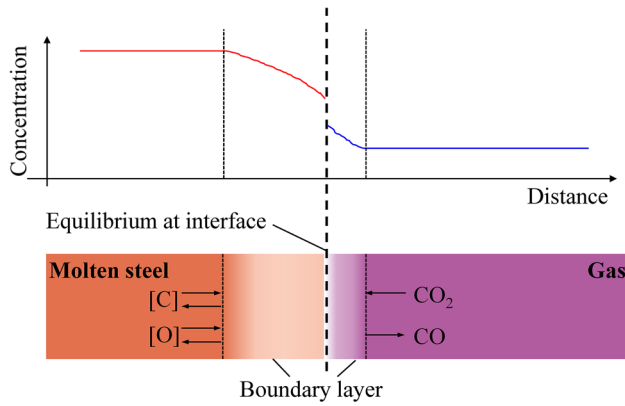


Fig. 5 Representation of decarburization steps with CO₂ injection at the interface

2.4 Chemical Reaction Rate

2.4.1 Decarburization at the Bubble, Bath, and Droplet Surfaces

According to the two-film theory, the decarburization process with CO₂ injection at the bubble, bath, and droplet surfaces involves the following steps: transports of dissolved C and O from the bulk steel to the reaction interface, transport of CO₂ gas from the bulk gas to the reaction interface, chemical reaction at the interface (including CO₂ adsorption, CO₂ decomposition, reaction of dissolved O produced by CO₂ decomposition or contained in molten steel itself with dissolved C to form CO, CO desorption, or CO gas produced by CO₂ decomposition further decomposes into dissolved C and O), transports of dissolved C and O from the reaction interface to the bulk steel, and transport of CO gas from the reaction interface to the bulk gas. This process is schematically illustrated in Fig. 5.

The chemical reaction at the gas–liquid interface is very rapid at steel temperature; thus, it is unlikely to be the rate-determining step. If the transports of dissolved C and O and the transports of CO₂ and CO gases are the rate-determining steps, the flux equations for dissolved element *E* and gas *G* can be written as

$$J_E = k_E(C_E - C_E^e) = \frac{k_E \rho_l}{M_E} ([wt\% E] - [wt\% E]^e) \quad (13)$$

$$J_G = k_G(C_G - C_G^e) = \frac{k_G}{RT} (P_G - P_G^e) \quad (14)$$

In Eqs. 13 and 14, *J* and *k* are the mass-transfer flux (mol/(m²·s)) and mass-transfer coefficient (m/s), respectively; ρ_l is the density of molten steel (kg/m³); *C* is the molar concentration (mol/m³); and *R* is the gas constant (*J*/

(mol·K)). The subscript *G* represents CO and CO₂ gases. Superscript *e* indicates the equilibrium concentration or equilibrium partial pressure at the interface, which was thermodynamically determined using Eqs. 1–6.

The chemical reaction rate of the dissolved element *E*, $v_{m,E}$, in basic Eqs. 9–12 can be obtained as follows:

$$v_{m,E} = A_m J_{m,E} \quad (15)$$

where *A_m* is the reaction area owing to decarburization at each site (m²).

Therefore, the CO and CO₂ partial pressures, reaction area, and mass transfer coefficient at each site are required to calculate the removal rate of the dissolved element *E*, which is described as follows:

2.4.1.1 Bubble Surface The partial pressure of gas *G* within a rising bubble is calculated as

$$P_G = P_{bubb} \cdot \frac{n_G}{n_{CO} + n_{CO_2}} \quad (16)$$

where *n_G* is the number of moles of gas *G* (mol), and the bubble pressure is obtained by

$$P_{bubb} = \rho_l g h_{bubb} + P_{vacc} + \frac{4\sigma_1}{d_{bubb}} \quad (17)$$

where *h_{bubb}* is the distance of CO₂ bubble to bath surface (m), *d_{bubb}* is the CO₂ bubble diameter (m), *P_{vacc}* is the vacuum chamber pressure (Pa), and σ_1 is the surface tension (N/m).

The reaction area at the bubble surface is the sum of the surface areas of all the CO₂ bubbles and is calculated as follows:

$$A_{bubb} = \sum_{n_{bubb}=1}^{n_{bubb,max}} 4\pi (r_{bubb})^2 \quad (18)$$

The number of bubbles, *n_{bubb}*, was calculated using the flow rate and the initial CO₂ bubble size. The initial bubble radius, *r_{bubb,0}*, [37] and bubble growth under reduced pressure [38] can be calculated by

$$r_{bubb,0} = 0.0455 \left(\frac{\sigma_l}{\rho_l} \right)^{0.5} (u_{bubb,0})^{0.44} \quad (19)$$

$$\frac{d^2 r_{bubb}}{dt^2} + \frac{3}{2r_{bubb}} \left(\frac{dr_{bubb}}{dt} \right)^2 = \frac{1}{\rho_l r_{bubb}} \left[(P_{vacc} + \rho_l g h_{bubb}) \left(\left(\frac{r_{bubb,0}}{r_{bubb}} \right)^3 - 1 \right) + \rho_l g u_{slip} t \right] \\ t = 0; \quad r_{bubb} = r_{bubb,0}; \quad \frac{dr_{bubb}}{dt} = 0 \quad (20)$$

where the *u_{slip}* is the bubble relative velocity estimated by Levich's equation [39].

$$u_{\text{slip}} \approx \left(\frac{4\sigma^2 g}{30\mu_1 \rho_1} \right)^{0.2} \quad (21)$$

The mass-transfer coefficients of dissolved elements E and gas G are calculated using Higbie's penetration theory [40] as follows:

$$k_E = \sqrt{\frac{2D_E u_{\text{slip}}}{\pi r_{\text{bubb}}}} \quad (22)$$

$$k_G = \sqrt{\frac{2D_G u_{\text{slip}}}{\pi r_{\text{bubb}}}} \quad (23)$$

where D_E is the diffusion coefficient, it is $2.24 \times 10^{-8} \text{ m}^2/\text{s}$ for dissolved C and $1.26 \times 10^{-8} \text{ m}^2/\text{s}$ for dissolved O [41]. The calculation of diffusion coefficient of gas G , D_G , can be found as described by Gu et al. [15]

2.4.1.2 Bath Surface The partial pressure of gas G at bath surface is calculated as

$$P_G = P_{\text{vacc}} \cdot \frac{n_G}{n_{\text{CO}} + n_{\text{CO}_2}} \quad (24)$$

According to Kitamura et al. [40], the reaction area at the activated bath surface can be ten times the geometric area, and this value has been adopted by many researchers [30, 42–44].

$$A_{\text{bath}} = 10\pi (r_{\text{vacc}})^2 \quad (25)$$

where r_{vacc} is the radius of the vacuum chamber.

The transports of CO and CO₂ are very fast under vacuum, and only the transports of dissolved C and O are considered as the rate-determining step for the decarburization reaction at the bath and droplet surfaces. The mass-transfer coefficient of dissolved C near the bath surface is 0.0015 m/s [42, 45], and that of dissolved O is calculated as [45]

$$k_O = k_C \sqrt{\frac{D_O}{D_C}} \quad (26)$$

2.4.1.3 Droplet surface The partial pressure of gas G at splash droplet surface is calculated using Eq. 24.

The size of the splash droplets in the vacuum chamber follows the Rosin–Rammler–Sperling distribution according to Koria and Lange [46], as follows:

$$R_{\text{wpd},k} = 100 \exp \left(- \left(\frac{d_{\text{drop},k}}{d_{\text{drop},\text{min}}} \right)^n \right) \quad (27)$$

$$n_{\text{drop},k} = \frac{m_{\text{drop}} \cdot R_{\text{drop},k}}{\rho_1 \frac{4}{3} \pi \left(\frac{d_{\text{drop},k}}{2} \right)^3} \quad (28)$$

According to Huang et al. [30], the droplet diameter is 0.3–8.7 mm, which can be divided into k ($k=21$) size classes with an interval of 0.42 mm. The $d_{\text{drop},k}$ is the droplet diameter of size class k (m), $d_{\text{drop},\text{min}}$ is the minimum diameter of the splash droplet (m), $R_{\text{wpd},k}$ is the weight percent of droplets with diameters larger than $d_{\text{drop},k}$ (%), $R_{\text{drop},k}$ and $n_{\text{drop},k}$ are the weight percent (%) and number of splash droplets with a diameter of $d_{\text{drop},k}$, respectively, m_{drop} is the weight of all the splash droplets (kg), and n is a parameter with a value of 1.3.

The reaction area at the droplet surface is the sum of the surface areas of all splash droplets, which is calculated in the following form:

$$A_{\text{drop}} = \sum_{k=1}^{21} n_{\text{drop},k} 4\pi \left(\frac{d_{\text{drop},k}}{2} \right)^2 \quad (29)$$

The mass-transfer coefficient of dissolved C for a droplet is 0.00031 m/s [47], and that of dissolved O is calculated using Eq. 26.

2.4.2 Decarburization of bulk steel

Unlike decarburization at the bubble, bath, and droplet surfaces, there is no initial interface for CO nucleation in bulk steel, and CO₂ is not involved. Decarburization can occur in bulk steel according to Eq. 3 only when the CO pressure is in excess of the hydrostatic pressure of molten steel and the surface tension effect [48, 49], and the critical CO pressure can be calculated by

$$P_{\text{CO},\text{crit}} = P_{\text{vacc}} + \rho_l g h_{\text{CO}} + \frac{2\sigma_1}{r_{\text{CO}}} \quad (30)$$

where h_{CO} is the distance between the CO bubble and the bath surface (m) and r_{CO} is the CO bubble radius (m), which is 0.0018 m [50].

The reaction rate of bulk steel can be calculated as follows [43]:

$$v_{\text{bulk},E} = \frac{w_V}{M_E} \left(k_{\text{CO},0} \frac{h_{\text{CO}}}{h_{\text{CO},0}} \right) (P^0 K_3 (f_C [\text{wt}\% \text{ C}]) (f_O [\text{wt}\% \text{ O}]) - P_{\text{CO}, \text{crit}}) \quad (31)$$

where $k_{\text{CO},0}$ is a constant, and it is $3 \times 10^{-7}/(\text{Pa}\cdot\text{s})$ when $h_{\text{CO},0}$ is 0.15 m [51].

2.4.3 FeO decomposition at the steel-slag interface

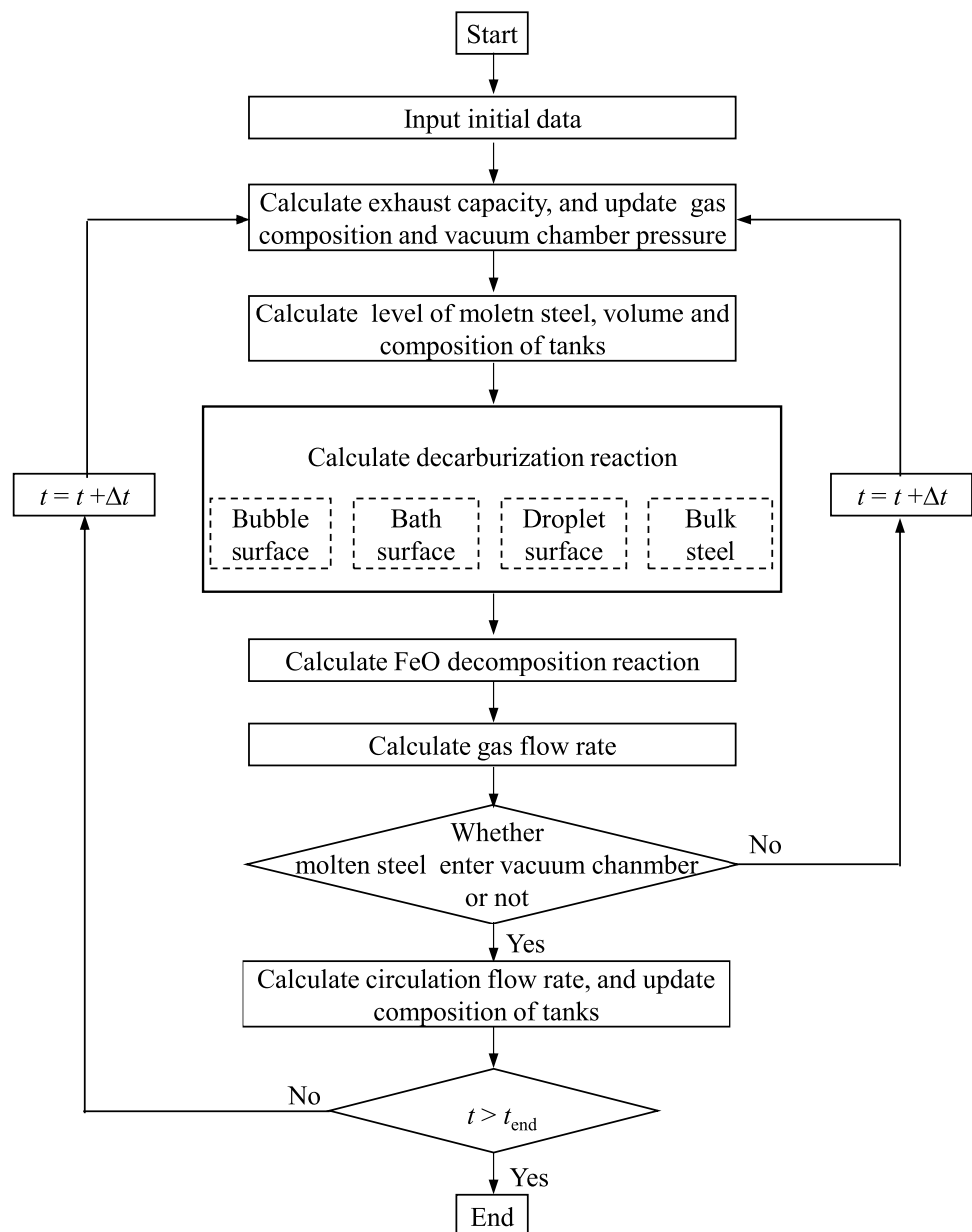
According to the two-film theory, the supply of oxygen from the RH slag to bulk steel involves the following steps: transport of FeO from the bulk slag to the steel-slag interface, FeO decomposition reaction, and transport of dissolved O from the steel-slag interface to the bulk steel.

When FeO transport is the rate-determining step during RH degassing [52], the reaction rate for the dissolved O can be written as

$$v_{\text{slag},O} = A_{\text{slag}} J_{\text{O}} = A_{\text{slag}} J_{\text{FeO}} = A_{\text{slag}} \frac{k_{\text{FeO}} \rho_{\text{slag}}}{M_{\text{FeO}}} ((\text{wt}\% \text{ FeO}) - (\text{wt}\% \text{ FeO})^e) \quad (32)$$

where A_{slag} is the interfacial area between molten steel and slag (m^2), M_{FeO} is the molar mass of FeO (kg/mol), ρ_{slag} is the slag density (kg/m^3), and k_{FeO} is the mass-transfer coefficient of FeO (m/s). The value of $k_{\text{FeO}} \rho_{\text{slag}}$ is 0.2–0.4 $\text{kg}/(\text{m}^2\cdot\text{s})$ for the RH slag at 1600 °C according to Sun and Mori [53], and the mean value of 0.3 is taken in this study.

Fig. 6 Flowchart for the calculation of RH decarburization process



2.5 Program and Computing Process

Mathematical simulation of RH decarburization with CO₂ injection is carried out by Visual Studio 2019 on a personal computer. A flowchart of the calculation of the RH decarburization process is shown in Fig. 6. The decarburization cycle, t_{end} , is set to 1100 s. The time step, Δt , is taken as 0.01 s, which is small enough to obtain a good convergence.

In this mathematical model, the variation of vacuum chamber pressure is calculated directly according to the pumping rate of vacuum pump, flow rate of CO₂ gas, generation of CO gas, and the consumption of CO₂ gas. For a given RH equipment, the pumping rate is a function of vacuum chamber pressure, and it is provided by manufacturer. Molten steel can enter the vacuum chamber and start to flow circularly only when the vacuum chamber pressure is lower than a certain value. Before circulation, decarburization reaction only occurs at the surface of CO₂ bubbles and the surface of molten steel in up-/down- snorkels. Therefore, the number and volume of tanks in each part are dynamically adjusted according to the level of molten steel at different vacuum chamber pressure. Once the vacuum chamber pressure is reduced to a working pressure, the number and

volume of tanks in each part remain unchanged as listed in Table 2.

3 Results and Discussion

3.1 Validation of Mathematical Model

To validate the present mathematical model, industrial experiments with two heats are carried out during the RH decarburization process of ultra-low-carbon steel. The initial compositions of the steel and slag and the type and flow rate of the lift gas are summarized in Table 3.

In the ultra-low-carbon steel refining process, molten steel is sampled manually at 1–2 min intervals from the RH ladle and analyzed using the CS-444 carbon/sulphur analyzer to determine the dissolved C content in the molten steel. The vacuum chamber pressure and dissolved O content are measured online. The variations in the vacuum chamber pressure and dissolved C and O contents in the RH degasser are shown in Figs. 7, 8, and 9, respectively, along with the predicted values.

Figure 7 shows that the vacuum chamber pressure, with a fore-vacuum pressure of 45–47 kPa, drops rapidly at the

Table 3 Initial composition of molten steel and slag

Heat	Lift gas	Flow rate (Nm ³ /h)	Element (ppm)		Steel mass (t)	Slag composition (wt%)				
			[C]	[O]		CaO	Al ₂ O ₃	FeO	MgO	SiO ₂
1	Ar	120–210	230	573	223	44.6	23.8	9.1	7.8	8.2
2	CO ₂	120–210	230	634	230	46.6	20.1	13.5	5.7	6.4

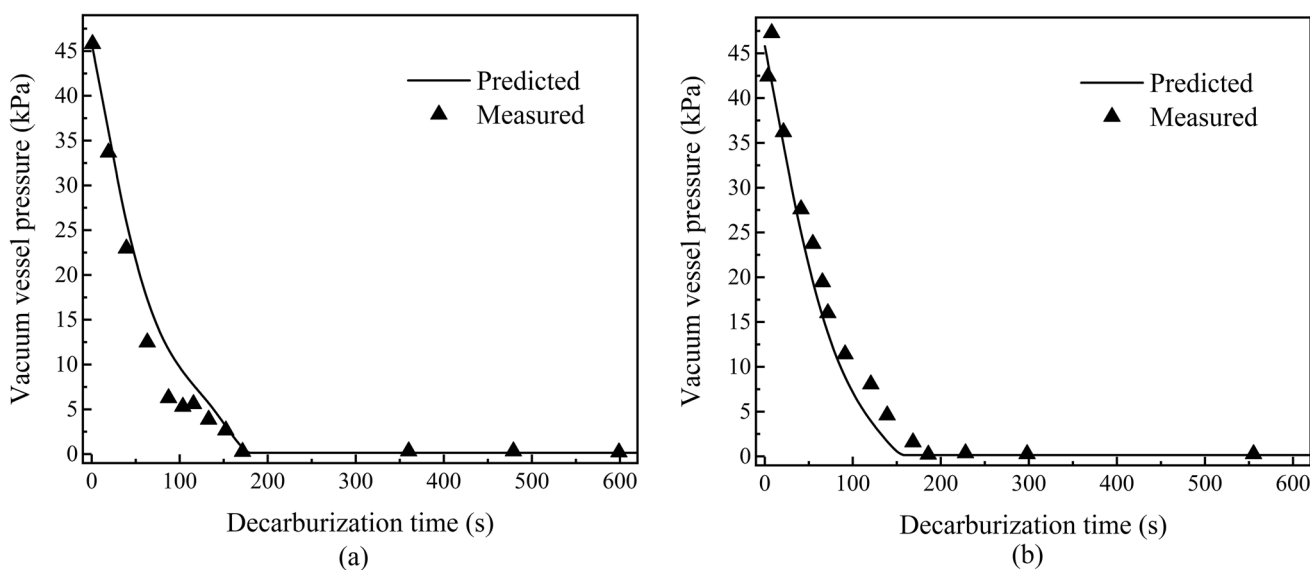


Fig. 7 Comparison of vacuum chamber pressure between predicted and measured results when the lift gas is **a** Ar and **b** CO₂

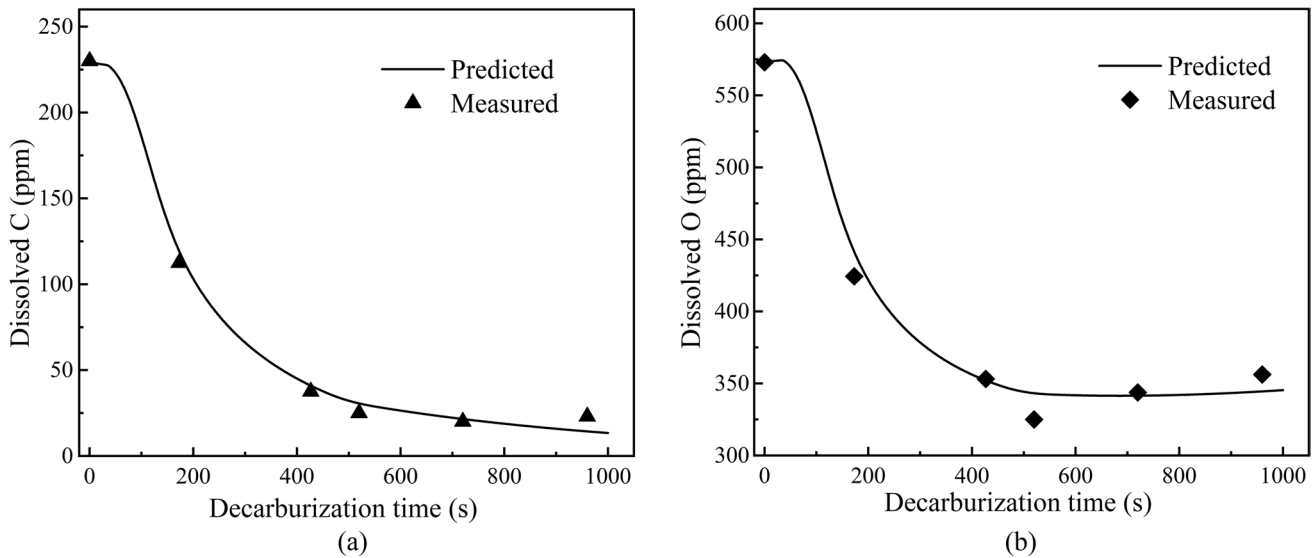


Fig. 8 Comparison of dissolved **a** C and **b** O contents in the RH degasser between predicted and measured results when the lift gas is Ar

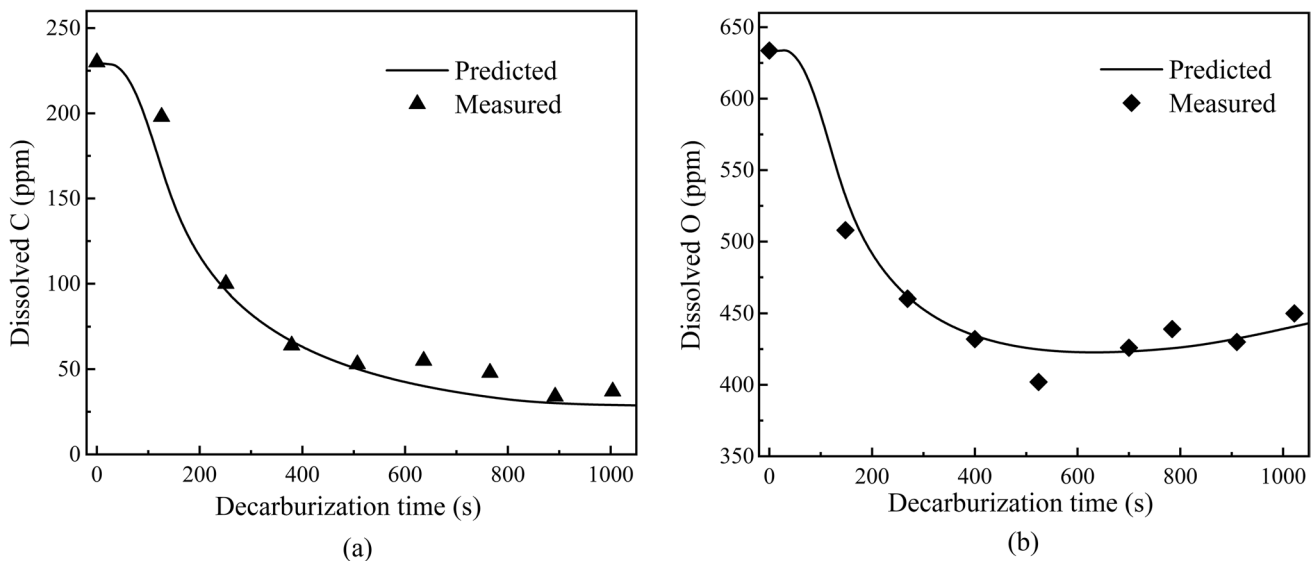


Fig. 9 Comparison of dissolved **a** C and **b** O contents in the RH degasser between predicted and measured results when the lift gas is CO₂

initial stage due to the vacuum pumping operation, and the working pressure of 0.2 kPa can be reached after about 3 min. Clearly, the variation in the vacuum chamber pressure calculated using the present mathematical model agrees well with the experimental results, regardless of the type of lift gas.

As shown in Figs. 8 and 9, the removal rates of dissolved C and O are relatively small in the first 1–2 min owing to the weak thermodynamic and kinetic conditions for the decarburization reactions caused by the high vacuum chamber pressure (Fig. 7). When the vacuum chamber

pressure is significantly lowered, the decarburization reactions, and thereby the removal rates of dissolved C and O, are greatly accelerated between 3 and 6 min. The removal rates of dissolved C and O are rather slow in the final stage of degassing because of the poor thermodynamic conditions caused by the ultra-low dissolved C content. Therefore, the RH decarburization process, which is mainly characterized by the variation in the dissolved C and O contents, can be reproduced well by the present mathematical model for both Ar and CO₂ injections.

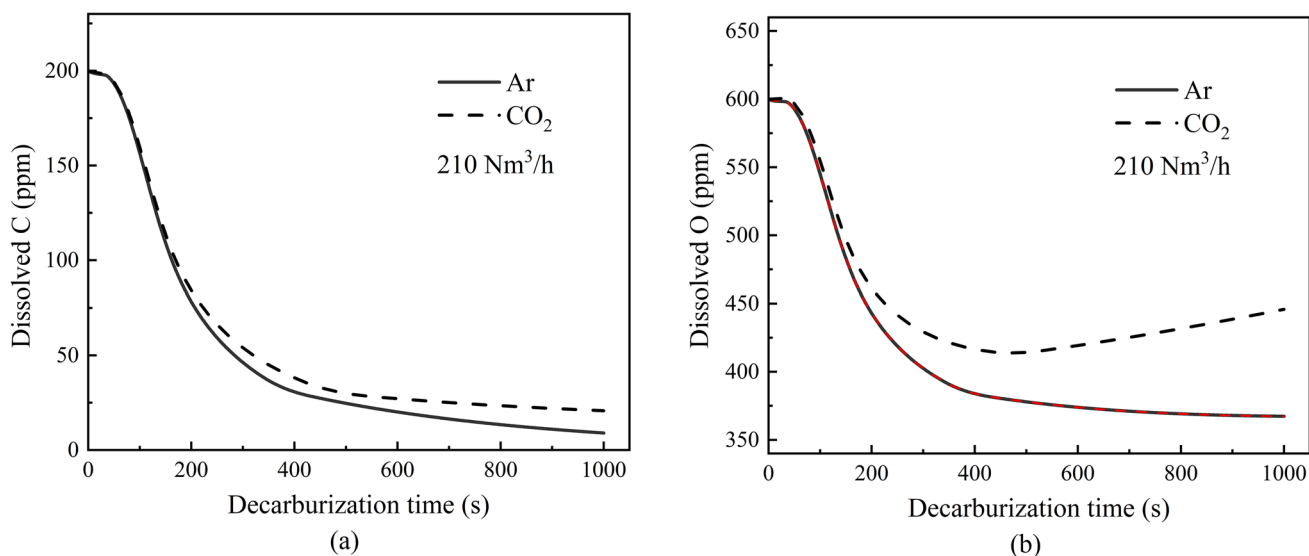


Fig. 10 Comparison of dissolved **a** C and **b** O contents in the RH degasser between Ar and CO₂ injections

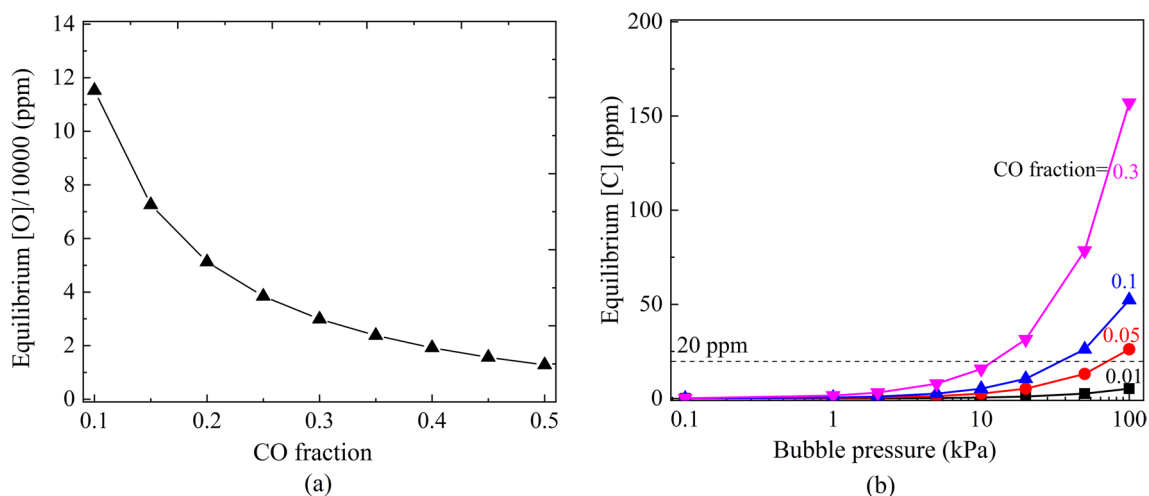


Fig. 11 **a** Equilibrium O content in molten steel at different CO volume fractions, and **b** Variation of equilibrium C content in molten steel as a function of bubble pressure at different CO fractions, where the actual [O] in molten steel is assumed to be 450 ppm

3.2 Decarburization Performance

To compare the decarburization performances of the Ar and CO₂ injections, mathematical simulations are performed when the initial dissolved C and O contents are 200 and 600 ppm, respectively, and the results are illustrated in Fig. 10.

It can be observed in Fig. 10 that for Ar injection, the dissolved C and O contents decrease rapidly in the early stage and continue to decrease slightly in the later stage. However, for CO₂ injection, an unexpected increase in the dissolved O content is observed, and the dissolved C content is higher than that for Ar injection in the middle and final stages. At the end of degassing, the dissolved C and O contents with CO₂ injection are 11 and 78 ppm greater than those with Ar

injection, respectively. To clarify the reasons for this, the related thermodynamics is calculated and given in Fig. 11, and the removal rate of the dissolved C and O resulting from the chemical reaction at the bubble surface is calculated and presented in Fig. 12.

With the rising of CO₂ bubble in the up-snorkel, the CO volume fraction inside the CO₂ bubble increases gradually, and the pressure inside the bubble, ($P_{CO_2} + P_{CO}$), reduces sharply from about 100 kPa to a pressure of the vacuum chamber. According to Eq. 1, the equilibrium O content in molten steel at different CO volume fractions can be calculated, as shown in Fig. 11a. Clearly, the Eq. 1 is dependent on the CO volume fraction rather than the bubble pressure, and the equilibrium O content increases remarkably with the

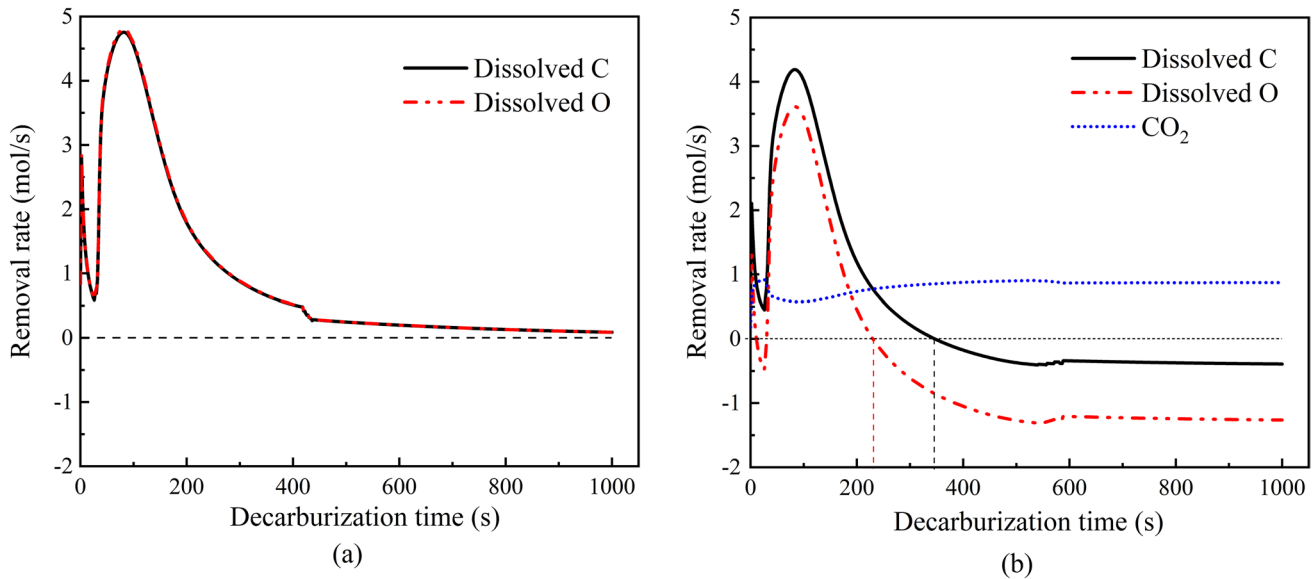


Fig. 12 Removal rate of dissolved C and O resulting from the chemical reaction at bubble surface when the lift gas is **a** Ar and **b** CO_2

reduction of CO volume fraction. The equilibrium O content exceeds ten thousand ppm easily, and it is much higher than the actual O content of 300–600 ppm in molten steel. Therefore, CO_2 can continuously decompose into CO and dissolved O and supply them to molten steel.

Depending on the thermodynamic conditions, the dissolved O produced by Eq. 1 can react with dissolved C in molten steel to form CO according to the forward reaction of Eq. 3 or the CO produced by Eq. 1 can further decompose into dissolved C and O according to the backward reaction of Eq. 3. Assuming the actual O content in molten steel is 450 ppm, the equilibrium C content as a function of bubble pressure can be calculated according to Eq. 3, as shown in Fig. 11b. Clearly, the equilibrium C content increases with the increase of bubble pressure or CO fraction, and the equilibrium C content at a higher bubble pressure or a larger CO fraction can easily exceed the actual C content of 20–50 ppm during the middle and final stages of RH decarburization process. In these two stages of RH decarburization, the CO produced by CO_2 decomposition can further decompose into dissolved C and O and supply them to molten steel when the CO_2 bubble locates in the middle and lower region of the up-snorkel where the bubble pressure is large.

As shown in Fig. 12, in comparison with Ar injection, a smaller removal rate of dissolved C and O at the bubble surface is observed for CO_2 injection, particularly the removal rate of dissolved O. The main reasons can be explained by the thermodynamics mentioned earlier in Fig. 11. First, CO_2 decomposition according to Eq. 1 leads to the continuous supply of dissolved O to molten steel; second, the reaction of dissolved C and O contained in the molten steel itself, according to the forward reaction of Eq. 3, is hindered by

the presence of CO produced by CO_2 decomposition. When the decarburization time is 230 s, the removal rate of the dissolved O at the bubble surface becomes negative (Fig. 12b), indicating that the formation rate of dissolved O in Eq. 1 is greater than that of consumption rate in Eq. 3. When the dissolved C content in molten steel is reduced to a certain value at 350 s, the removal rate of dissolved C at the bubble surface becomes negative (Fig. 12b), indicating that the CO produced by CO_2 decomposition further decomposes into dissolved C and O according to the backward reaction of Eq. 3. It should be noted that the forward and backward reactions of Eq. 3 can occur simultaneously at a certain time mainly depending on the vertical location of CO_2 bubble in up-snorkel (namely, the bubble pressure), as shown in Fig. 11b. Therefore, the variation rate of dissolved C and O in Fig. 12b is the comprehensive results of chemical reactions at the surface of all CO_2 bubbles.

As mentioned above, the removal rates of the dissolved C and O at the bubble surface become negative at 230 and 350 s, respectively, when CO_2 is injected as a lift gas. However, for the entire RH degasser, the removal rate of dissolved O becomes negative at 500 s, whereas that of dissolved C always remains positive, as shown in Fig. 13a. This is because the removal rates of the dissolved C and O at other sites (bath surface, droplet surface, and bulk steel) are always positive, as shown in Fig. 13b.

3.3 Effect of Initial Dissolved O Content

The decarburization performance largely depends on the initial dissolved O content of the molten steel. The changes

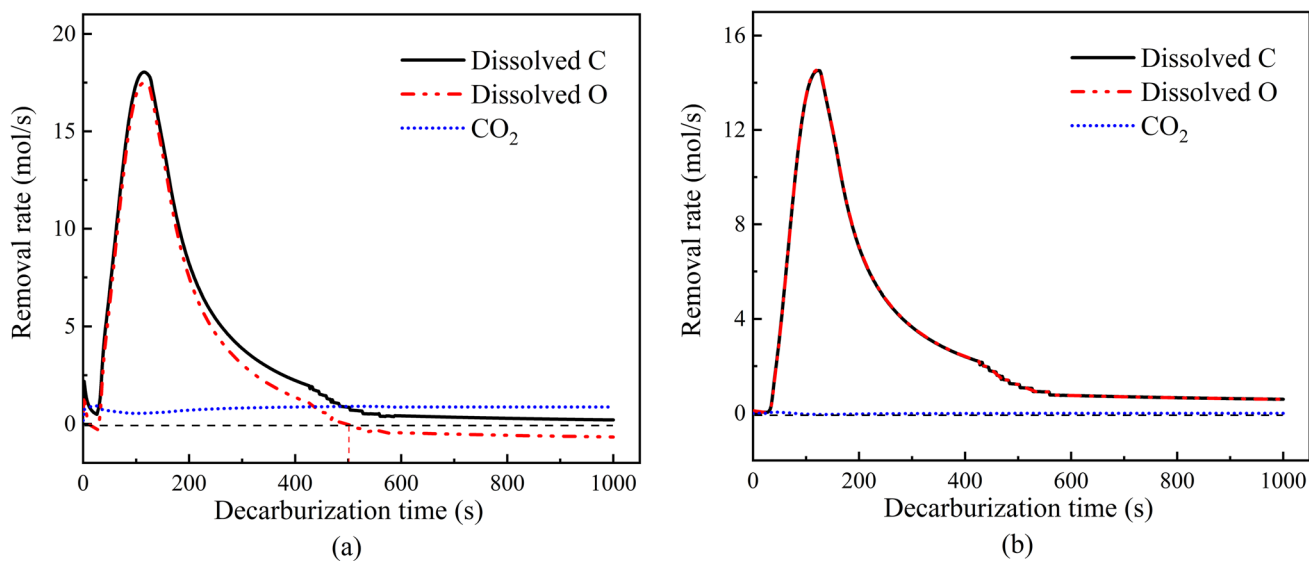


Fig. 13 Removal rate of dissolved C and O **a** in the whole RH degasser, and **b** at other sites (bath surface, droplet surface and bulk steel) when the lift gas is CO₂

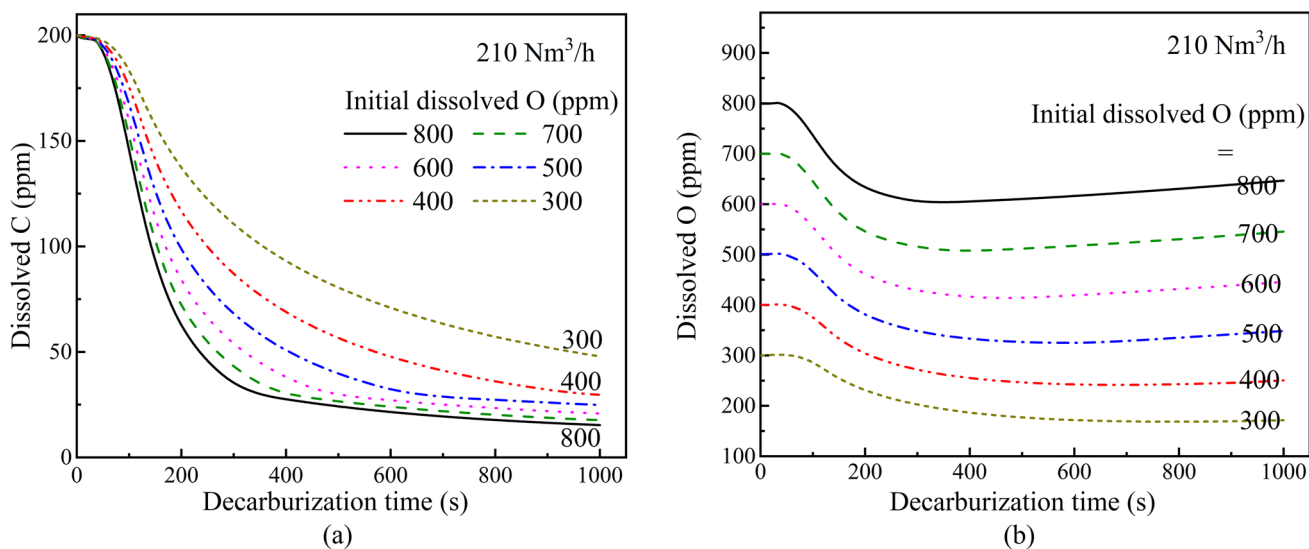


Fig. 14 Change of dissolved **a** C and **b** O in the RH degasser with different initial dissolved O contents when the initial dissolved C is 200 ppm

in the dissolved C and O contents in the RH degasser with different initial dissolved O contents are calculated and are illustrated in Fig. 14, when the initial dissolved C content is 200 ppm and CO₂ is injected.

Figure 14 shows that the dissolved C content at the end of the RH degassing decreases remarkably from 48 to 15 ppm, and the final dissolved O content increases significantly from 172 to 647 ppm when the initial dissolved O content increases from 300 to 800 ppm. As expected, a higher initial dissolved O content is beneficial for achieving a lower dissolved C content at the end of the RH degassing. Therefore, the initial dissolved O content should be reasonably controlled when CO₂

is injected as a lift gas. For instance, the initial dissolved O content should be at least 600 ppm if the dissolved C content at the end is less than 20 ppm when the initial dissolved C content is 200 ppm.

3.4 Switching from CO₂ to Ar Injection

As discussed earlier, the final dissolved O content after the CO₂ injection is much higher than that after the Ar injection, regardless of the initial dissolved O content. A higher dissolved O content in the molten steel means that more Al needs to be added for subsequent deoxidation, and more

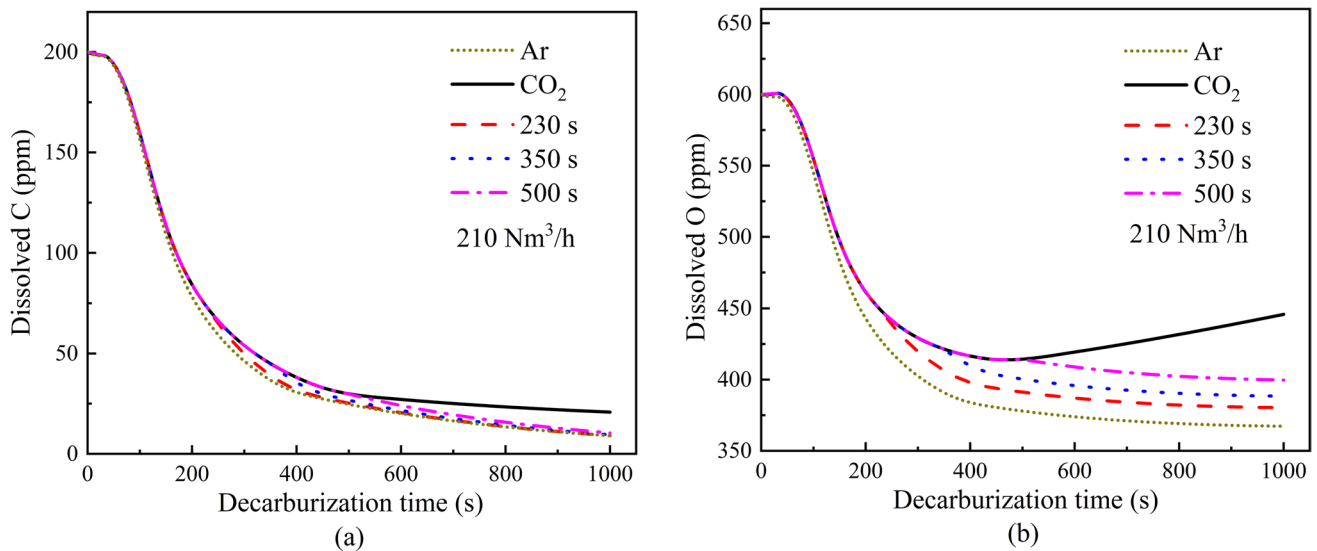


Fig. 15 Change of dissolved **a** C and **b** O contents in the RH degasser at different switching times

Al₂O₃ inclusions will be produced. Therefore, the lift gas is suggested to be switched from CO₂ to Ar at a certain moment.

Figure 15 shows the changes in dissolved C and O contents in the RH degasser at different switching times. Evidently, not only the final dissolved O content but also the final dissolved C content can be significantly reduced. Specifically, the final dissolved C content decreases from 20 to 10.4, 9.5, and 9.1 ppm, and the final dissolved O content decreases from 446 to 400, 388, and 380 ppm when the switching times are 500, 350, and 230 s, respectively. The final dissolved C and O contents at a switching time of 230 s are very close to the values obtained with pure Ar injection (9 and 367 ppm, respectively). The appropriate switching time depends on the final dissolved C and O contents required.

4 Conclusion

In this study, a mathematical model, based on tanks-in-series model, is built to study RH decarburization when CO₂ is injected as a lift gas during the ultra-low-carbon steel degassing process. Decarburization reaction at the bubble surface, bath surface, droplet surface, and bulk steel are selected, and the influence of variation of vacuum chamber pressure on decarburization is considered. Industrial experiments are conducted to validate the model. A comparison of decarburization between CO₂ and Ar injections is discussed. The effects of the initial dissolved O content and switching operations from CO₂ to Ar injection on the decarburization performance are also presented. The main conclusions are as follows:

- 1 The model predictions are consistent with the variations in vacuum chamber pressure and dissolved C and O contents measured from industrial experiments, confirming that the RH decarburization process can be reasonably reproduced by the mathematical model.
- 2 Higher final dissolved C and O contents with CO₂ injection are observed in comparison with Ar injection. The final dissolved C and O contents are 20 and 446 ppm for CO₂ injection, while they are 9 and 367 ppm for Ar injection, respectively.
- 3 A higher initial dissolved O content is beneficial for obtaining a lower final dissolved C content with CO₂ injection. Ar can be completely substituted by CO₂ to meet the requirement of a final dissolved C content of less than 20 ppm when the initial dissolved O content is greater than or equal to 600 ppm and the initial dissolved C content is 200 ppm.
- 4 Pure CO₂ can be switched to pure Ar during the middle stage of degassing if lower final dissolved C and O contents are required.

Acknowledgements This work was supported by the National Natural Science Foundation of China (Grant No. 52104321), the Natural Science Foundation of Chongqing, China (Grant No. CSTB2023N-SCQ-MSX0871), and the Science and Technology Research Program of Chongqing Municipal Education Commission (Grant No. KJQN202101404).

Declarations

Conflict of interest The authors declare no conflicts of interest.

References

1. Y. Zhang, L. Yu, K. Cui, H. Wang, T. Fu, *Chem. Eng. J.* **455**, 140552 (2023). <https://doi.org/10.1016/j.cej.2022.140552>
2. H. Zhang, W. Sun, W. Li, G. Ma, *Appl. Energ.* **309**, 118485 (2022). <https://doi.org/10.1016/j.apenergy.2021.118485>
3. Q. Chen, Y. Gu, Z. Tang, W. Wei, Y. Sun, *Appl. Energ.* **220**, 192 (2018). <https://doi.org/10.1016/j.apenergy.2018.03.043>
4. S. Yun, M. Jang, J. Kim, *Energy* **229**, 120778 (2021). <https://doi.org/10.1016/j.energy.2021.120778>
5. K. Dong, X. Wang, *Metals* **9**, 273 (2019). <https://doi.org/10.3390/met9030273>
6. C. Feng, R. Zhu, R. Liu, K. Dong, G. Wei, *Steel Res. Int.* **92**, 2000704 (2021). <https://doi.org/10.1002/srin.202000704>
7. H. Zhang, Z. Yuan, L. Mei, X. Peng, K. Liu, H. Zhao, *J. Sustain. Metall.* **8**, 1803 (2022). <https://doi.org/10.1007/s40831-022-00607-8>
8. G. Wei, C. Zhou, S. Hu, J. Tian, R. Zhu, D. Wang, Q. Zhu, *Metals* **12**, 1457 (2022). <https://doi.org/10.3390/met12091457>
9. H. Liu, J. Liu, S. Johannes, F. Penz, L. Sun, R. Zhang, *Z. An. Metall. Mater. Trans. B* **51**, 756 (2020). <https://doi.org/10.1007/s11663-020-01776-1>
10. R. Zhu, B. Han, K. Dong, G. Wei, *Int. J. Min. Met. Mater.* **27**, 1421 (2020). <https://doi.org/10.1007/s12613-020-2065-5>
11. G. Wei, R. Zhu, S. Yang, X. Wu, K. Dong, *Ironmak. Steelmak.* **48**, 703 (2021). <https://doi.org/10.1080/03019233.2021.1896068>
12. G. Wei, R. Zhu, T. Tang, K. Dong, X. Wu, *Metall. Mater. Trans. B* **50**, 1077 (2019). <https://doi.org/10.1007/s11663-018-1482-6>
13. G. Zhou, R. Wei, J. Zhu, J. CO₂Util. **60**, 102016 (2022). <https://doi.org/10.1016/j.jcou.2022.102016>
14. Y. Zhou, G. Wei, R. Zhu, K. Dong, *Sep. Purif. Technol.* **315**, 123693 (2023). <https://doi.org/10.1016/j.seppur.2023.123693>
15. Y. Gu, H. Wang, R. Zhu, J. Wang, M. Lv, H. Wang, *Steel Res. Int.* **85**, 589 (2014). <https://doi.org/10.1002/srin.201300106>
16. J. Zhang, L. Liu, X. Zhao, S. Lei, Q. Dong, *ISIJ Int.* **54**, 1560 (2014). <https://doi.org/10.2355/isijinternational.54.1560>
17. M. Wang, J. Guo, X. Li, C. Yao, Y. Bao, *Vacuum* **185**, 109984 (2021). <https://doi.org/10.1016/j.vacuum.2020.109984>
18. Y. Kim, K. Yi, *Met. Mater. Int.* **25**, 238 (2019). <https://doi.org/10.1007/s12540-018-0160-1>
19. S. Chen, H. Lei, H. Hou, C. Ding, H. Zhang, Y. Zhao, *J. Mater. Res. Technol.* **15**, 5141 (2021). <https://doi.org/10.1016/j.jmrt.2021.10.118>
20. D. Geng, J. Zheng, K. Wang, P. Wang, R. Liang, H. Liu, H. Lei, J. He, *Metall. Mater. Trans. B* **46**, 1484 (2015). <https://doi.org/10.1007/s11663-015-0314-1>
21. H. Ling, L. Zhang, *Metall. Mater. Trans. B* **49**, 2709 (2018). <https://doi.org/10.1007/s11663-018-1319-3>
22. C. Liu, L. Zhang, Y. Sun, W. Yang, *Metall. Mater. Trans. B* **53**, 670 (2022). <https://doi.org/10.1007/s11663-022-02434-4>
23. Y. Zhu, R. Zhu, X. Wang, *Ind. Heat.* **46**, 7 (2017). <https://doi.org/10.3969/j.issn.1002-1639.2017.06.002>
24. B. Han, R. Zhu, Y. Zhu, R. Liu, W. Wu, Q. Li, G. Wei, *Metall. Mater. Trans. B* **49**, 3544 (2018). <https://doi.org/10.1007/s11663-018-1417-2>
25. B. Han, G. Wei, R. Zhu, W. Wu, J. Jiang, C. Feng, J. Dong, S. Hu, R. Liu, *J. CO₂Util.* **34**, 53 (2019). <https://doi.org/10.1016/j.jcou.2019.05.038>
26. G. Wei, B. Han, R. Zhu, *Chin. J. Eng.* **42**, 203 (2020). <https://doi.org/10.13374/j.issn2095-9389.2019.06.30.001>
27. B. Han, R. Zhu, C. Feng, W. Li, G. Wei, Z. Wang, Q. Li, *Vacuum* **179**, 109520 (2020). <https://doi.org/10.1016/j.vacuum.2020.109520>
28. G. Chen, J. Yang, L. Li, M. Zhang, S. He, *J. CO₂Util.* **50**, 101586 (2021). <https://doi.org/10.1016/j.jcou.2021.101586>
29. G. Chen, J. Yang, L. Li, M. Zhang, S. He, *Iron & Steel* **57**, 55 (2022). <https://doi.org/10.13228/j.boyuan.issn0449-749x.20210526>
30. Y. Huang, G. Cheng, Q. Wang, S. Li, W. Dai, *Ironmak. Steelmak.* **47**, 655 (2020). <https://doi.org/10.1080/03019233.2019.1567999>
31. D. Zhan, Y. Zhang, H. Jiang, H. Zhang, *J. Iron. Steel Res. Int.* **25**, 409 (2018). <https://doi.org/10.1007/s42243-018-0053-z>
32. D. Mukherjee, A. Shukla, D. Senk, *Ironmak. Steelmak.* **45**, 412 (2018). <https://doi.org/10.1080/03019233.2016.1274847>
33. J. Wang, P. Ni, C. Chen, M. Ersson, Y. Li, *Int. J. Min. Met. Mater.* **30**, 844 (2023). <https://doi.org/10.1007/s12613-022-2558-5>
34. R. Wang, J. Yu, H. Cui, *Metall. Mater. Trans. B* **53**, 342 (2022). <https://doi.org/10.1007/s11663-021-02371-8>
35. H. Nomura, K. Mori, *Tran. ISIJ* **13**, 325 (1973). <https://doi.org/10.2355/isijinternational1966.13.325>
36. Y. Ji, C. Liu, H. Yu, X. Deng, F. Huang, X. Wang, *J. Iron. Steel Res. Int.* **27**, 402 (2020). <https://doi.org/10.1007/s42243-019-00285-z>
37. M. Sano, K. Mori, Y. Fujita, *Tetsu-to-Hagané* **65**, 1140 (1979). [https://doi.org/10.1016/0036-9748\(86\)90199-7](https://doi.org/10.1016/0036-9748(86)90199-7)
38. J. Szekely, G. Martins, *Trans. Met. Soc. AIME.* **245**, 629 (1969)
39. V. Levich, *Physicochemical Hydrodynamics* (Prentice-Hall Inc., Englewood Cliffs, 1962)
40. R. Higbie, *Trans. AICHE* **31**, 365 (1935)
41. K. Peng, C. Liu, L. Zhang, Y. Sun, *Metall. Mater. Trans. B* **53**, 2004 (2022). <https://doi.org/10.1007/s11663-022-02519-0>
42. M. Van Ende, Y. Kim, M. Cho, J. Choi, I. Jung, *Metall. Mater. Trans. B* **42**, 477 (2011). <https://doi.org/10.1007/s11663-011-9495-4>
43. S. Chen, H. Lei, M. Wang, *Steel Res. Int.* **92**, 2100032 (2021). <https://doi.org/10.1002/srin.202100032>
44. S. Chen, H. Lei, M. Wang, B. Yang, L. Dai, Y. Zhao, *Vacuum* **167**, 255 (2019). <https://doi.org/10.1016/j.vacuum.2019.06.018>
45. T. Kitamura, K. Miyamoto, R. Tsujino, S. Mizoguchi, K. Kato, *ISIJ Int.* **36**, 395 (1996). <https://doi.org/10.2355/isijinternational.36.395>
46. S. Koria, K. Lange, *Metall. Mater. Trans. B* **15**, 109 (1984). <https://doi.org/10.1007/BF02661068>
47. P. Wu, Y. Yang, M. Barati, A. McLean, *Metall. Mater. Trans. B* **45**, 2211 (2014). <https://doi.org/10.1007/s11663-014-0126-8>
48. G. Chen, S. He, *Ind. Eng. Chem. Res.* **58**, 18855 (2019). <https://doi.org/10.1021/acs.iecr.9b03932>
49. Z. You, G. Cheng, X. Wang, Z. Qin, J. Tian, J. Zhang, *Metall. Mater. Trans. B* **46**, 459 (2015). <https://doi.org/10.1007/s11663-014-0182-0>
50. T. Kuwabara, K. Umezawa, K. Mori, H. Watanabe, *Trans. ISIJ* **28**, 305 (1988)
51. M. Takahashi, H. Matsumoto, T. Saito, *ISIJ Int.* **35**(12), 1452 (1995). <https://doi.org/10.2355/isijinternational.35.1452>
52. Y. Qin, X. Wang, L. Li, F. Huang, *Steel Res. Int.* **86**, 1037 (2015). <https://doi.org/10.1002/srin.201400349>
53. H. Sun, K. Mori, *ISIJ Int.* **36**, 34 (1996). https://doi.org/10.2355/isijinternational.36.Suppl_S34

Publisher's Note Springer Nature remains neutral with regard to jurisdictional claims in published maps and institutional affiliations.

Springer Nature or its licensor (e.g. a society or other partner) holds exclusive rights to this article under a publishing agreement with the author(s) or other rightsholder(s); author self-archiving of the accepted manuscript version of this article is solely governed by the terms of such publishing agreement and applicable law.